Room-temperature magnetic skyrmions in Pt/Co/Cu multilayers

Shuyu Cheng,[1] Núria Bagués,[2] Camelia M. Selcu,[1,*] Jacob B. Freyermuth,[1] Ziling Li,[1] Binbin Wang,[2] Shekhar Das,[1] P. Chris Hammel,[1] Mohit Randeria,[1] David W. McComb,[2,†] and Roland K. Kawakami[1,‡]

[1]*Department of Physics, The Ohio State University, Columbus, Ohio 43210, USA*

[2]*Department of Materials Science and Engineering, The Ohio State University, Columbus, Ohio 43210, USA*

(Received 3 March 2023; revised 19 October 2023; accepted 20 October 2023; published 20 November 2023)

Magnetic skyrmions are promising for next-generation information storage and processing owing to their potential advantages in data storage density, robustness, and energy efficiency. The magnetic multilayers consisting of Pt, Co, and a third metal element X provide an ideal platform to study skyrmions due to their highly tunable magnetic properties. Here, we report the observation of room-temperature bubblelike Néel skyrmions in epitaxial Pt/Co/Cu multilayers in samples with multidomain states in zero field. The magneto-optic Kerr effect and a superconducting quantum interference device magnetometry are applied to investigate the shapes of the hysteresis loops, the magnetic anisotropy, and the saturation magnetization. By tuning the Co thickness and the number of periods, we achieve perpendicular and in-plane magnetized states and multidomain states that are identified by a wasp-waisted hysteresis loop. Skyrmions are directly imaged by magnetic force microscopy and Lorentz transmission electron microscopy. The development of room-temperature skyrmions in Pt/Co/Cu multilayers may lead to advances in skyrmion-related research and applications.

DOI: 10.1103/PhysRevB.108.174433

I. INTRODUCTION

Magnetic skyrmions are topologically protected spin textures that stand out as one of the strongest candidates for next-generation information storage due to their small sizes, thermal stability, and high energy efficiency [1–4]. These special spin textures originate from the complex interplay between exchange stiffness, magnetic anisotropy, dipolar interactions, applied field, and the Dzyaloshinskii-Moriya interaction (DMI). The DMI plays an important role in the stabilization of skyrmions, as it favors perpendicular alignment between neighboring spins [5,6]. From a material point of view, the DMI is allowed by asymmetric crystal structures, which occur in bulk crystals that are noncentrosymmetric and at interfaces due to the broken mirror plane symmetry [7–9]. While the former gives rise to Bloch skyrmions in which the spins twist in the tangential direction [10,11], the latter gives rise to Néel skyrmions in which the spins tumble in the radial direction [12,13]. Though less common, Néel skyrmions could also form in bulk crystals when a mirror plane symmetry is broken [14].

Since 2009, magnetic skyrmions have been discovered in a variety of materials, including B20-phase materials [10,11,15], two-dimensional materials [16,17], and magnetic bilayers and multilayers [12,13,18,19]. Among these materials, Pt/Co/X (X = metallic material) magnetic multilayers have drawn much attention because the insertion of the X layers into Pt/Co superlattices generates noncanceling interfacial DMI by breaking the inversion symmetry [12,20,21]. Furthermore, the magnetic properties of Pt/Co/X multilayers can be vastly tuned by varying the thickness of each layer [22,23] and the number of repetitions of Pt/Co/X [24,25] or simply changing the element X [26,27]. The magnetic properties of Pt/Co/X multilayer systems with various metallic materials X, including X = Mn [28], Ni [29], Cu [22], Ru [30], Ho [31], Ta [13], W [24], Ir [12], etc., have been report. Among the options for transition metal X, Cu is of particular interest for a number of reasons. Since the lattice constant of Cu is close to that of Co and Pt, it is possible to grow Pt/Co/Cu multilayers epitaxially along the Pt(111) direction [22]. This enables the layer-by-layer growth of high-quality crystalline Pt/Co/Cu multilayers using molecular beam epitaxy (MBE). Previous studies also reported that Pt/Co/Cu multilayers have no magnetic dead layer compared to those with other materials for the X layer [26]. For these reasons, Pt/Co/Cu could be a model system to investigate skyrmion properties.

In this paper, we report the observation of room-temperature bubblelike Néel skyrmions in epitaxial Pt/Co/Cu multilayers, which was achieved by applying an out-of-plane (OOP) magnetic field to samples with a zero-field multidomain state. We used the magneto-optic Kerr effect (MOKE) and magnetic force microscopy (MFM) to investigate how the zero-field magnetic states depend on the Co thickness t_{Co} and number of periods N. We observed a spin-reorientation transition from OOP magnetized to multidomain to in-plane (IP) magnetized with increasing t_{Co} and a transition from OOP magnetized to multidomain with increasing N. The multidomain states of interest could be recognized by the wasp-waisted shapes of their OOP MOKE loops, and applying an OOP field generated skyrmions, as observed by Lorentz transmission electron microscopy (LTEM) and MFM. In addition, since we developed the growth of epitaxial $[Pt/Co/Cu]_N$ multilayers on an insulating substrate, we were able to apply current pulses which assisted in the nucleation of skyrmions.

*selcu.1@osu.edu
†mccomb.29@osu.edu
‡kawakami.15@osu.edu

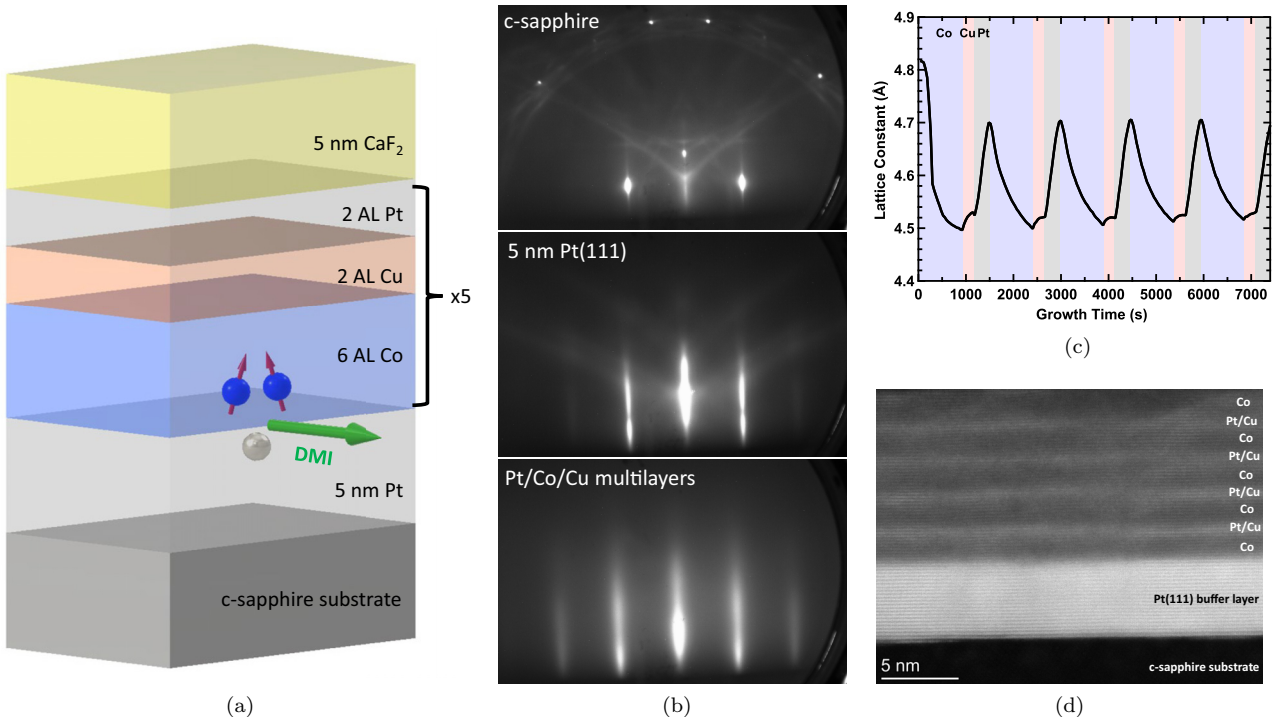

FIG. 1. Material growth and structural characterization. (a) Schematic drawing of the sample structure. (b) *In situ* RHEED patterns during growth. Top: sapphire(0001) with the beam along the $[11\bar{2}0]$ in-plane direction. Middle: Pt(111). Bottom: $[Pt(2)/Co(6)/Cu(2)]_5$ multilayers. (c) In-plane lattice constant extracted from the RHEED streak spacing during the growth. The blue, red, and gray regions correspond to the deposition of Co, Cu, and Pt, respectively. (d) STEM-HAADF image of $[Pt(2)/Co(6)/Cu(2)]_5$ multilayers.

To better understand the properties of the skyrmions and the multidomain states, we employed micromagnetic simulations which were able to reproduce the skyrmion size, the domain size in the multidomain state, and the transition from an OOP magnetized state to a multidomain state with increasing N.

II. GROWTH AND STRUCTURAL CHARACTERIZATIONS

The $[Pt/Co/Cu]_N$ multilayers were grown on epitaxial Pt(111) buffer layers on $Al_2O_3(0001)$ substrates (MTI Corporation) using MBE. Unless otherwise noted, the structure of the multilayer samples is (from bottom to top) 5 nm Pt/[6 atomic layers (AL) Co/2 AL Cu/2 AL Pt]$_5$/5 nm CaF_2 (hereafter $[Pt(2)/Co(6)/Cu(2)]_5$, where the sequence of the layers is from the bottom to the top and the numbers in the parentheses represent the thickness of each layer in units of atomic layers), as shown in Fig. 1(a). Prior to growth, the $Al_2O_3(0001)$ substrates were annealed in air at 1000 °C for 180 min and then degassed in the growth chamber at 500 °C for 30 min. A 5 nm Pt(111) buffer layer was epitaxially grown on the $Al_2O_3(0001)$ substrate following the recipe described in [32]. $[Pt/Co/Cu]_N$ multilayers were deposited on top of the Pt(111) buffer layer at room temperature by opening and closing the shutters sequentially. The growth time for each layer was determined by the growth rate, which was calibrated by a quartz crystal deposition monitor. Pt was deposited from an electron-beam evaporator, while Co and Cu were deposited from Knudsen cells. The typical growth rates for Pt, Co, and Cu are 0.9, 0.8, and 1.0 Å/min, respectively. After growth, 5 nm CaF_2 was deposited on the sample to protect the sample from oxidation. The *in situ* reflection high-energy electron diffraction (RHEED) pattern was monitored during the growth, as shown in Fig. 1(b). Streaky RHEED patterns indicate that the $[Pt(2)/Co(6)/Co(2)]_5$ multilayers grow epitaxially. Furthermore, the in-plane lattice constant extracted from the RHEED pattern during growth shows oscillatory behavior, with a decreasing lattice constant during Co layer growth and an increasing lattice constant during Cu and Pt layer growth, as shown in Fig. 1(c). This oscillation of the in-plane lattice constant does not decay during growth.

The structure of the sample was confirmed by scanning transmission electron microscopy (STEM) imaging of a cross-section sample using a ThermoFisher probe-corrected Themis-Z at 300 kV. The cross-section sample was prepared by Ga ion milling at 30 and 5 kV using a focused ion beam (FIB). Figure 1(d) shows a STEM high-angle annular dark field (HAADF) image of a $[Pt(2)/Co(6)/Co(2)]_5$ multilayer on top of a Pt buffer layer on Al_2O_3 viewed along the Al_2O_3 $[1\bar{1}00]$ axis. In Fig. 1(d), the $[Pt(2)/Co(6)/Co(2)]_5$ sample exhibits well-defined layered structures. Due to the atomic number Z contrast in the HAADF images the Co layers appear as dark layers in the STEM image, while the Pt and Cu layers appear as bright layers. While there is clear modulation of the intensity in the HAADF image, we cannot differentiate between the relative influence of interdiffusion and interface roughness in the heterostructure.

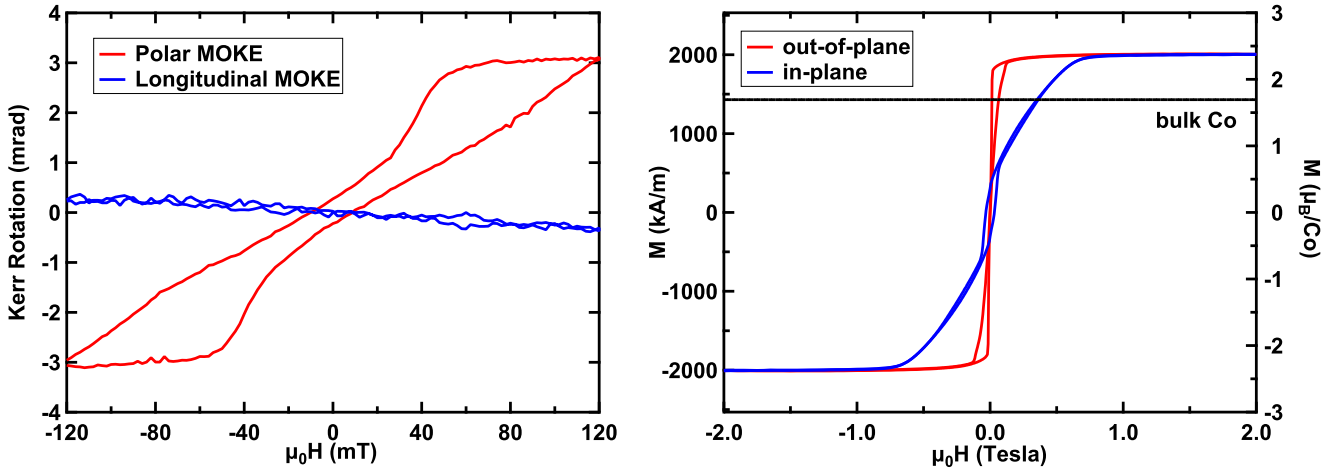

FIG. 2. Magnetic characterizations of $[Pt(2)/Co(6)/Cu(2)]_5$ multilayers. (a) MOKE hysteresis loops of $[Pt(2)/Co(6)/Cu(2)]_5$ multilayers. (b) SQUID hysteresis loops of $[Pt(2)/Co(6)/Cu(2)]_5$ multilayers. The black solid line represents 1430 kA/m, which is the saturation magnetization of bulk Co.

III. MAGNETIC CHARACTERIZATIONS

We first discuss MOKE and superconducting quantum interference device (SQUID) measurements of $[Pt(2)/Co(6)/Cu(2)]_5$ multilayers. The MOKE measurement utilized a 632.8 nm laser and employed normal incidence for polar loops and a 45° angle of incidence for longitudinal loops. Figure 2(a) shows the polar (red curve) and longitudinal (blue curve) MOKE hysteresis loops of a $[Pt(2)/Co(6)/Cu(2)]_5$ multilayer. The polar MOKE hysteresis loop shows a "wasp-waisted" shape with small remanence. Although the applied magnetic field was limited to 120 mT, which is not sufficient to fully saturate the sample, the hysteresis loop nevertheless captures the main magnetic characteristics of the sample. Fully saturated loops were measured by SQUID [Fig. 2(b)] and are discussed below. The wasp-waisted shape of the hysteresis loop is similar to that of Pt/Co/Cu multilayers near the spin-reorientation transition (SRT), where magnetic stripe domains with an OOP easy axis were observed [22]. Meanwhile, the longitudinal MOKE hysteresis loop shows almost linear behavior in the 120 mT range, with a much smaller magnitude compared to polar MOKE. The response to external magnetic fields where the magnetization is easier to polarize out of plane compared to in plane is due to the presence of the perpendicular surface magnetic anisotropy from the Pt/Co interfaces.

The results from the SQUID measurements of $[Pt(2)/Co(6)/Cu(2)]_5$ are shown in Fig. 2(b). The out-of-plane hysteresis loop (red curve) shows a shape similar to the polar MOKE loop, with low remanence and a saturation field of 192 mT, while the in-plane hysteresis loop (blue curve) saturates at ∼0.7 T. We note that the saturation magnetization of $[Pt(2)/Co(6)/Cu(2)]_5$ multilayers is measured to be 2010 ± 200 kA/m, where the uncertainty is mainly from the uncertainty in the film thickness (∼10%). This is larger than the bulk Co value (1430 kA/m) [33] by the amount of $\Delta M_{Co} = 580 \pm 200$ kA/m. The additional magnetic moment comes from Pt and is induced by the magnetic proximity effect, which has been reported in Pt/Co multilayers [34]. To quantify this effect, we calculate the magnetic moment of Pt from the following formula [34]:

$$\Delta M_{Co}\, t_{Co}^{total} = M_{Pt}\, t_{Pt}^{total}. \quad (1)$$

Since most of the Pt moment concentrates in the first two atomic layers of Pt adjacent to the Co layers [35], here, we take the thickness of 10 atomic layers of Pt, i.e., 2.3 nm, as t_{Pt}^{total}. By substituting $t_{Co}^{total} = 6.1 \pm 0.6$ nm and $t_{Pt}^{total} = 2.3 \pm 0.2$ nm into Eq. (1), we get $M_{Pt} = 2.6 \pm 0.7 \mu_B$/Pt.

To tune the hysteresis loop shape and magnetic anisotropy, we varied the Co thickness and the number of periods N. For these studies, we maintained a constant thickness of 2 AL for the Pt and Cu layers.

Beginning with the Co thickness, we synthesized a sample series with $t_{Co} = 4$, 5, 6, 7, 8, and 9 AL for a fixed number of periods $N = 5$. Representative polar (red curve) and longitudinal (blue curve) MOKE loops are shown in Fig. 3(a). At a low Co thickness of 4 AL (sample I), the polar loop is square with a large remanence, while the longitudinal loop has a small signal with no remanence. This indicates a perpendicular (out-of-plane) magnetic easy axis. As t_{Co} increases, the polar MOKE hysteresis loop evolves to a wasp-waist shape with low remanence for $t_{Co} = 6$ AL (sample III) and, eventually, to almost linear with negligible hysteresis and zero remanence for $t_{Co} = 8$ AL. Meanwhile, the longitudinal MOKE hysteresis loop exhibits increasing remanence with thickness, going from zero remanence for $t_{Co} = 4$ and 6 AL to a loop with substantial remanence and sharp magnetization reversals for 8 AL. This indicates a transition to in-plane magnetization for thicker Co. This spin-reorientation transition from perpendicular magnetization to in-plane magnetization with increasing Co thickness is summarized by the horizontal circles at $N = 5$ in Fig. 3(e), with red circles signifying perpendicular magnetization, green circles signifying the multidomain SRT region (the domain structure is verified by MFM and LTEM elsewhere in this paper), and blue circles signifying in-plane magnetization.

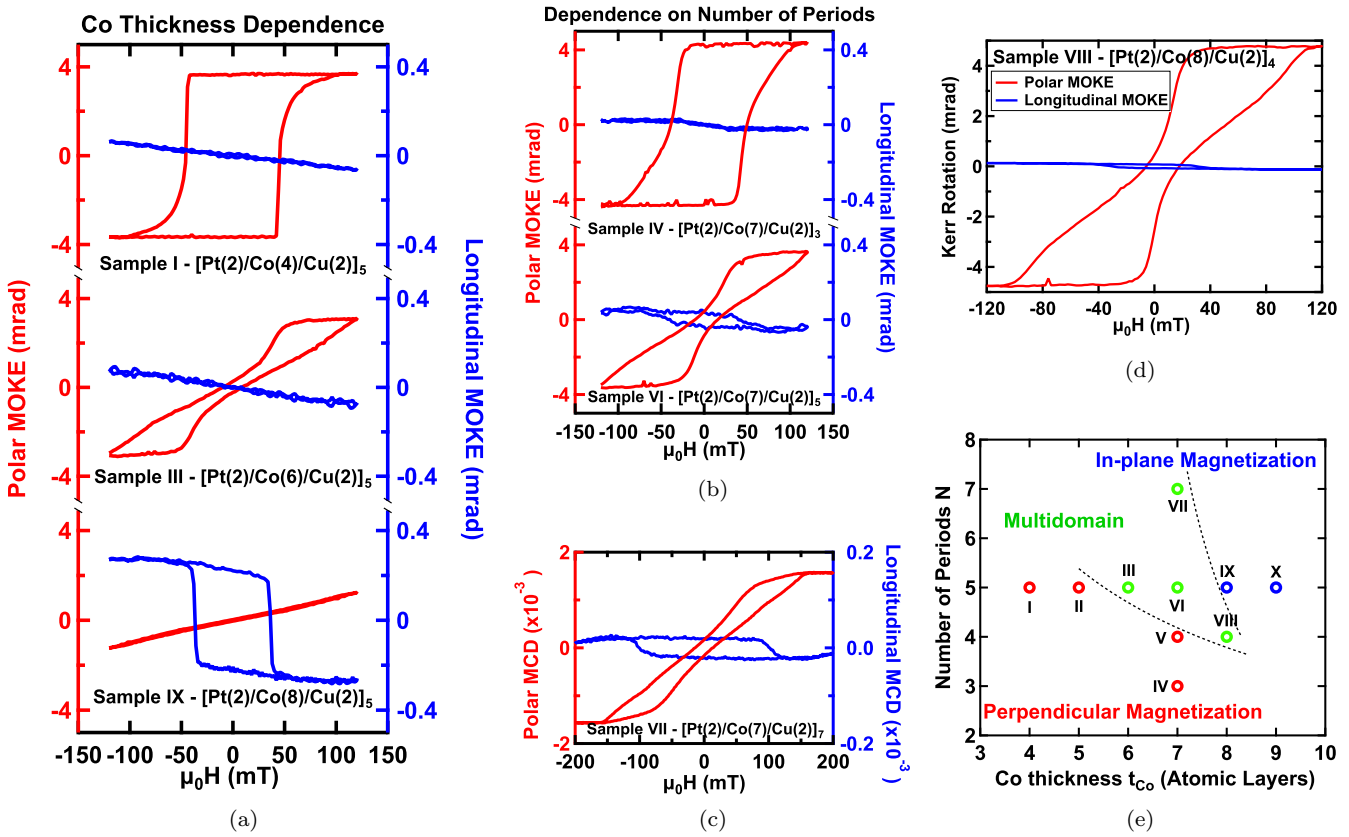

FIG. 3. Relationship between MOKE hysteresis loops and the multilayer structure. (a) Representative polar (red curve) and longitudinal (blue curve) MOKE hysteresis loops of $[Pt(2)/Co(t_{Co})/Cu(2)]_5$ multilayers with a fixed number of periods $N = 5$. (b) Representative polar (red curve) and longitudinal (blue curve) MOKE hysteresis loops of $[Pt(2)/Co(7)/Cu(2)]_N$ multilayers with fixed Co layer thickness $t_{Co} =$ 7 AL. (c) Polar (red curve) and longitudinal (blue curve) MCD hysteresis loops of $[Pt(2)/Co(7)/Cu(2)]_7$ (sample VII) acquired on another setup. (d) Polar (red curve) and longitudinal (blue curve) MOKE hysteresis loops of $[Pt(2)/Co(8)/Cu(2)]_4$ (sample VIII). (e) Summary of the sample series. The dashed lines are guides to the eye.

This thickness-dependent spin reorientation is understood as a competition between the perpendicular magnetic anisotropy (PMA) originating from the Pt/Co interface and the magnetic shape anisotropy favoring in-plane magnetization [36]. The Pt/Co PMA is interfacial, so its energy density scales inversely with Co thickness. On the other hand, the shape anisotropy is bulklike, so its energy density remains constant as Co thickness is varied. Thus, larger thicknesses will favor in-plane magnetization, while smaller thicknesses will favor perpendicular magnetization. We estimated the spin-reorientation thickness d_{Co} of an individual Co layer by balancing the uniaxial anisotropy and magnetic dipolar energy [see Sec. S2 in the Supplemental Material (SM) for details] [37]. Taking the magnetocrystalline anisotropy of hcp-structured cobalt $K_{MC} = 0.43 \times 10^6\,J/m^3$ from [38] and interfacial anisotropy $K_S = 0.9 \times 10^{-3}\,J/m^2$ from the analysis of our SQUID data, the spin-reorientation thickness of cobalt is estimated to be 1.7 nm. This is in good agreement with our experimental results.

The hysteresis loops also exhibit variation as a function of the number of periods N of the Pt/Co/Cu multilayer. Figure 3(b) shows the out-of-plane and in-plane hysteresis loops for $[Pt(2)/Co(7)/Cu(2)]_N$ for $N = 3$, 5, and 7. In this sample series, sample IV with three periods has a polar MOKE loop (red curve, top loop) with nearly 100% remanence and a longitudinal MOKE loop (blue curve, top loop) with a weak response, indicating perpendicular magnetization. For sample VI with five periods, the polar MOKE loop (red curve, bottom loop) has a wasp-waisted shape, and the longitudinal MOKE loop shows a small signal with nonzero remanence. Similar to the wasp-waisted polar loops in Fig. 2(a) and sample III in Fig. 3(a), the loop is not fully saturated, so these are minor loops. Nevertheless, the applied field goes sufficiently high to reveal the wasp-waisted loop corresponding to a multidomain state (see MFM in the SM, Sec. S4) [37]. The easy axis is predominantly OOP, but the presence of hysteresis in the longitudinal loop (blue curve, middle loop) suggests the emergence of a small in-plane magnetization component.

For sample VII with seven periods, we measured the hysteresis loops on a different magneto-optic setup with higher magnetic fields to saturate the magnetization fully. Here, we measured magnetic circular dichroism (MCD) using a 532 nm laser at a 45° angle of incidence. As shown in the bottom panel of Fig. 3(b), the polar MCD measurement (red curve) exhibits an elongated wasp-waisted loop that saturates at ∼170 mT. The longitudinal MCD measurement (blue curve) shows the presence of an in-plane component of magnetization.

TABLE I. Summary of the structures and zero-field magnetic states of the samples.

Sample	Co thickness t_{Co}	Number of periods N	Zero-field magnetic state
I	4	5	OOP
II	5	5	OOP
III	6	5	Multidomain
IV	7	3	OOP
V	7	4	OOP
VI	7	5	Multidomain
VII	7	7	Multidomain
VIII	8	4	Multidomain
IX	8	5	IP
X	9	5	IP

These loops are characteristic of a multidomain state, which was directly confirmed by MFM (see SM, Sec. S4) [37]. We note that the presence of multidomains for large N is consistent with prior MOKE microscopy measurements of Pt/Co/Cu samples with $N = 10$ [22]. The transition from a perpendicularly magnetized state with high remanence at low N to a multidomain structure with tilted hysteresis loops at higher N has been known for Pt/Co [39–41] and was observed more recently in Pt/Co/X superlattices [42]. This transition is likely due to stronger dipolar fields, and hence stronger dipolar couplings that drive the stabilization of domains, as N increases. It is also worth noting that such dipolar fields could play an important role in stabilizing skyrmions [43,44]. This transition was also reproduced by our micromagnetic simulations, as discussed later.

To further investigate the boundary of the multidomain region, we synthesized a sample with $t_{Co} = 8$ AL and $N = 4$ (sample VIII), which is to the lower right of multidomain sample VI in the N-t_{Co} diagram [Fig. 3(e)]. The polar and longitudinal MOKE loops for this sample [Fig. 3(d)] confirm the wasp-waisted polar loop that is characteristic of a multidomain state.

The zero-field magnetic states of the samples are summarized in Table I, and the hysteresis loops of each sample are shown in Sec. S1 of the SM [37].

IV. LTEM AND MFM MEASUREMENTS

We now focus on the samples in the transition region with wasp-waisted polar hysteresis loops, indicated by the green circles in Fig. 3(e) (and labeled "Multidomain"). Here, we employed LTEM and MFM to image the magnetic domain structure and investigate the possible presence of skyrmions. For the LTEM measurements [45], FIB milling was utilized to thin the sapphire substrate, thus allowing the electron beam to transmit through the sample. Figures 4(a)–4(c) show planar-view LTEM images of a $[Pt(2)/Co(6)/Cu(2)]_5$ multilayer sample at various out-of-plane magnetic fields. The straight parallel lines are from the substrate thinning and are not due to magnetic textures. For these images, we have tilted the sample by 20° to achieve magnetic contrast for Néel skyrmions [20,46].

Beginning at zero field [Fig. 4(a)], we observe labyrinth magnetic domains which evolve into magnetic stripe domains when the field is ramped up to 100 mT [Fig. 4(b)]. When the field is raised to 135 mT [Fig. 4(c)], several magnetic bubbles are observed. The images in Figs. 4(a)–4(d) have improved contrast after we subtract a background image taken in the field-polarized state at 160 mT [47].

These bubbles are identified as Néel skyrmions based on the following considerations. First, there is no magnetic contrast when the electron beam is normally incident on the sample, which is the expected behavior since the Lorentz force is purely tangential for Néel skyrmions. Second, the magnetic contrast appears when the sample is tilted, and the bubble appears to have a positive lobe and a negative lobe, which is the expected shape for Néel skyrmions [20]. Section S3 of the SM provides a detailed explanation of the LTEM contrast [37], which depends on the sample tilt and not the skyrmion chirality. A line cut across the lobes, shown in Fig. 4(e) (see the SM, Sec. S3, for line-cut profiles at different fields) [37], establishes the size of the bubble is approximately 120 nm at 135 mT.

We further investigate the magnetic domain structure and skyrmion spin textures using MFM. An advantage of MFM over LTEM is that sample preparation including substrate thinning is not required. This provides access to the as-grown magnetic properties, as substrate thinning could introduce strain. In addition, MFM measurements are compatible with devices fabricated by photolithography and electron-beam lithography. The measurements were performed on a Bruker MFM equipped with a homemade variable magnet with an out-of-plane field range of −115 to 115 mT. The [Pt/Co/Cu] multilayers were patterned to have micron-wide device channels.

Upon investigating samples in the multidomain region of the phase diagram [green circles in Fig. 3(e)], we found that skyrmions could be nucleated using either field ramp sequences or current pulses. For a $[Pt(2)/Co(6)/Cu(2)]_5$ sample [Figs. 5(a)–5(c)], the out-of-plane magnetic field was first set to −100 mT. Ramping to 0 mT produced labyrinth magnetic domains in the channel [Fig. 5(a)]. Fast Fourier transform (FFT) analysis of the MFM image yields an average labyrinth domain width of 130 nm at zero field. As the field was increased to 67 mT, the domain structure evolved to magnetic stripe domains with a lower density of domain walls [Fig. 5(b)], consistent with the domain structures observed by LTEM [Fig. 4(b)]. As the MFM magnet is unable to reach the 135 mT needed to nucleate skyrmions, we decided to use

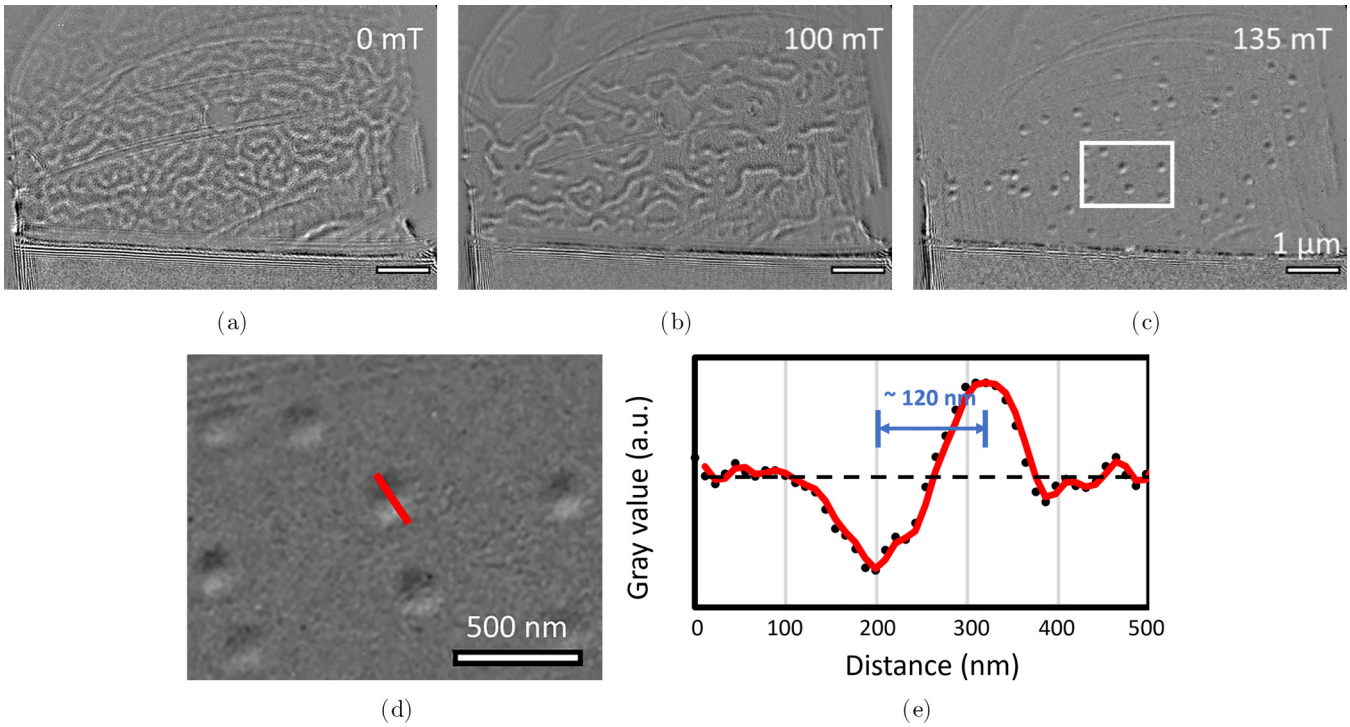

FIG. 4. LTEM images of the $[Pt(2)/Co(6)/Cu(2)]_5$ thin film with a thinned substrate. LTEM images of the $[Pt(2)/Co(6)/Cu(2)]_5$ sample under (a) 0 mT, (b) 100 mT, and (c) 135 mT applied magnetic field. The scale bar represents 1 μm. (d). Zoomed-in LTEM image at 135 mT. The area of this image corresponds to the white box in (c). The scale bar represents 500 nm. A background image taken in the field-polarized state (160 mT) is subtracted from (a)–(d) to improve the contrast. (e). Line-cut profile of a single skyrmion along the direction of the red line in (d). The red solid line is a smoothed curve of the line-cut profile.

current pulses to help nucleate the skyrmions, as demonstrated previously in other materials [13,48–50]. Following a single current pulse of 1.39×10^{12} A/m^2 with a duration of 20 ns, some of the stripe domains break up into isolated skyrmions [Fig. 5(c)].

For a $[Pt(2)/Co(8)/Cu(2)]_4$ sample, the saturation field is within the range of the MFM magnet, so we investigate skyrmion nucleation by field ramping. Starting by applying a −100 mT field, we ramp up through 0 mT to a final field of 115 mT. Figures 5(d)–5(g) show MFM images at representative fields. At 70 mT, the magnetic texture is dominated by stripe domains, and a few skyrmions are observed. Increasing to 92.5 mT causes many of the stripes to nucleate into skyrmions or disappear altogether. At 100 mT, some of the

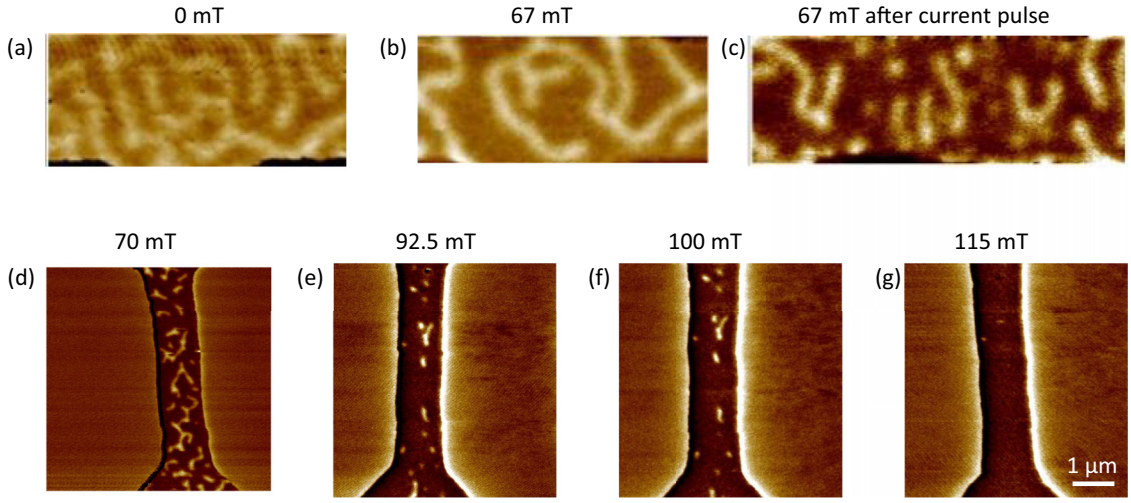

FIG. 5. MFM images of skyrmions. (a) For a $[Pt(2)/Co(6)/Cu(2)]_5$ sample, the magnetic field is ramped from −100 to 0 mT, leading to labyrinth domains; (b) ramping to 67 mT produces domains with lower density, and (c) application of a current pulse generates isolated skyrmions. For a $[Pt(2)/Co(8)/Cu(2)]_4$ sample, the magnetic field is ramped from −100 mT to (d) 70 mT, (e) 92.5 mT, (f) 100 mT, and (g) 115 mT. With increasing field, magnetic textures evolve from stripe domains to skyrmions to a field-polarized state.

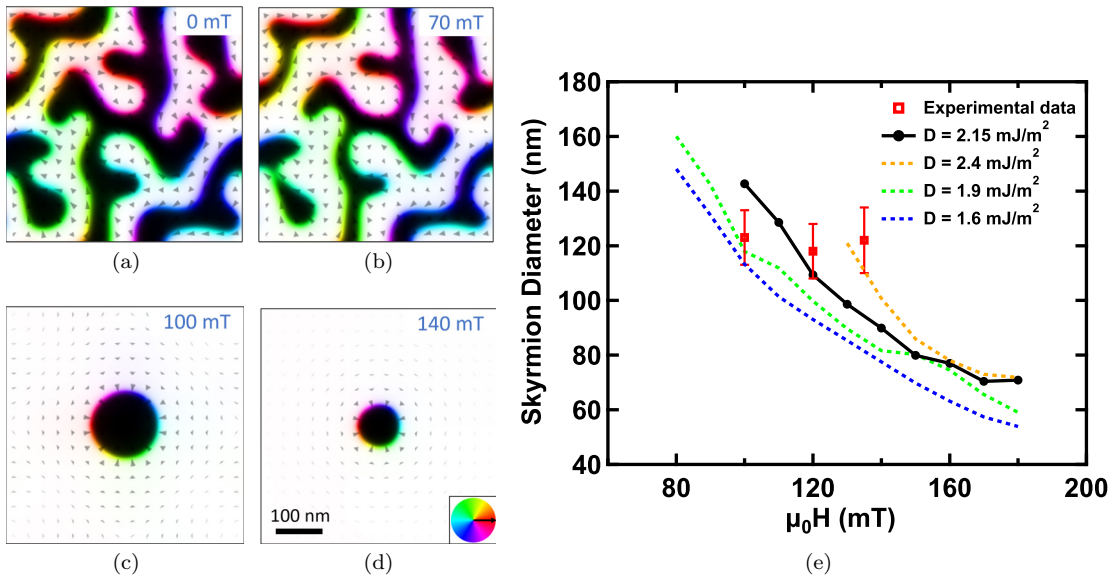

FIG. 6. Micromagnetic simulation of a $[Pt(2)/Co(6)/Cu(2)]_5$ sample with (a) 0 mT, (b) 70 mT, (c) 100 mT, and (d) 140 mT applied field. The color wheel represents the in-plane component of the magnetization direction. (e) Simulated diameter of skyrmions as a function of applied field using several different DMI values. The red squares represent experimental data from LTEM measurements (see SM Section S3 for line-cut profiles at different fields) [37].

skyrmions have disappeared, along with the stripes. Finally, at 115 mT, most of the sample has become field polarized.

Additional MFM measurements establish the presence of skyrmions in a $[Pt(2)/Co(7)/Cu(2)]_5$ sample (SM, Sec. S4) [37].

V. MICROMAGNETIC SIMULATIONS

Micromagnetic simulations using MUMAX3 [51] were performed to try to understand two important aspects of $[Pt/Co/Cu]_N$ multilayers: the out-of-plane ferromagnetic domain to multidomain transition and the size of skyrmions. In our simulations, the $[Pt(2)/Co(6)/Cu(2)]_N$ was modeled as a $3N$-layer stack, with the magnetic moments of the Co and Pt layers, the exchange coupling between the neighboring Co and Pt layers, and interlayer exchange coupling between neighboring Co layers taken into consideration. The interlayer exchange coupling between Co layers through Pt/Cu was set to be ∼10% of the exchange coupling within Co layers [35]. The micromagnetic parameters used were an exchange stiffness A_{ex} of 25 pJ/m [52–54], a uniaxial anisotropy K_u of 1.2 MJ/m^3, a DMI strength D of 2.15 mJ/m^2 from [55], and saturation magnetizations M_S of 1.4×10^6 and 1.7×10^6 A/m for Co and Pt layers, respectively. The selection of each micromagnetic parameter is justified in Sec. S5 in the SM [37].

We first investigated the transition from uniformly magnetized states to multidomain states as the number of periods N increases. In these simulations, the initial state was magnetized along the out-of-plane direction, with 1% of spins randomized to avoid unstable equilibrium states. Then the system was allowed to relax from the initial state at zero field. For $N = 1$ to 4, the magnetization remains uniformly magnetized at zero field, while for $N = 5$, the uniformly magnetized state breaks into labyrinth domains at zero field (see the SM, Sec. S5, for details) [37]. This is because as N increases, the dipolar interaction increases and overcomes the exchange interaction that favors a uniformly magnetized state [43,44,49]. FFT analysis yields a labyrinth domain width of 120 nm at zero field, in good agreement with the MFM data.

Many different values of A_{ex} were found in the literature, ranging from 10 to 35 pJ/m [52–54,56–60]. To investigate the influence of A_{ex} on multidomain formation, we lowered A_{ex} from 25 to 10 pJ/m, which is another widely used value [56]. With the smaller exchange stiffness, all of the $[Pt(2)/Co(6)/Cu(2)]_N$ multilayers relaxed into multidomain states because such a small exchange stiffness is not sufficient to maintain a uniformly magnetized state (see the SM, Sec. S5, for details) [37]. In addition, with $A_{ex} = 10$ pJ/m, the simulated labyrinth domain width is 55 nm, much smaller than the experimentally observed value. Therefore, the agreement of simulation and experiment for 25 pJ/m but not for 10 pJ/m indicates the exchange stiffness of cobalt in our samples is close to 25 pJ/m.

We next studied the skyrmion size and its dependence on various parameters using the same micromagnetic model. In these simulations, we relax the system to equilibrium starting with an initial condition of a Néel skyrmion with an ∼75 nm diameter. Results of the simulations for the $[Pt(2)/Co(6)/Cu(2)]_5$ sample are shown in Fig. 6. At zero field, the simulations show a labyrinth domain structure, consistent with both the MFM and LTEM [Fig. 6(a)]. As the magnetic field is increased, Néel skyrmions can be stabilized starting around 80–90 mT. Continuing to increase the field causes the skyrmions to shrink, as shown in Figs. 6(c) and 6(d). Compared with experimental values of the skyrmion size that show little variation with field [red squares in Fig. 6(e)], the simulated skyrmion size exhibits a stronger variation with field than is consistent with the experimental uncertainties (see the SM, Sec. S3, for details on the analysis) [37]. The

reason for this discrepancy is unclear. Nevertheless, the experimental values of the skyrmion size near 120 nm suggest that the value of the DMI falls between 1.9 and 2.4 $\mathrm{mJ/m^2}$ [see Fig. 6(e)]. Another trend observed in the simulation is an increase in the skyrmion size with increasing values of D. These simulated dependences of skyrmion size on D and magnetic field are in agreement with previous analytical results by Wang *et al.* [61]. While our study supports a D value of $\sim$2 $\mathrm{mJ/m^2}$, we note that another study suggested a D value below $\sim$1 $\mathrm{mJ/m^2}$ [27]. However, our simulations (see the SM, Sec. S5, for details) show that this smaller value of D would result in skyrmions much smaller than the 120 nm observed in experiments [37].

The variation of skyrmion size with D is understood as follows. Intuitively, a skyrmion can be thought of as being composed of an inner "core" region with magnetization antiparallel to the applied field and an intermediate "wall" region where the magnetization rotates until it becomes parallel to the applied field in the "outside" region. The Zeeman energy is most important in the core and outside regions, so increasing the field will shrink the core and increase the outside ferromagnetic region to lower the Zeeman energy, which leads to a smaller skyrmion. The DMI is most important in the wall region, so with a larger D, the skyrmion can lower its overall energy by increasing the width of the wall even though the Zeeman and anisotropy energies will increase. Thus, the skyrmion size will get larger with increasing D.

VI. CONCLUSIONS

In conclusion, we observed room-temperature skyrmions in $[\mathrm{Pt/Co/Cu}]_N$ multilayers. By varying the number of periods N and the Co thickness, we tuned the magnetic state from perpendicularly magnetized to multidomain (wasp-waisted loop shape) to in-plane magnetized. Magnetic imaging by LTEM and MFM on multidomain samples showed that the magnetic spin texture evolves from labyrinth domains at low perpendicular magnetic fields to isolated skyrmion spin textures at higher fields. By tilting the sample during LTEM, we verified that the skyrmions are Néel type. MFM measurements on patterned devices showed that current pulses could nucleate skyrmions at lower magnetic fields compared to only ramping magnetic fields. While our imaging studies focused on the multidomain samples, we do not exclude the possibility of skyrmions in the OOP or IP magnetized samples. This work establishes Pt/Co/Cu multilayers as a model system for investigating room-temperature skyrmions in ultrathin epitaxial materials.

ACKNOWLEDGMENTS

We acknowledge stimulating discussions with D. Pelekhov. This work was supported by the DARPA TEE program under Grant No. D18AP00008. Z.L. was supported by AFOSR/MURI project 2DMagic Grant No. FA9550-19-1-0390 and U.S. Department of Energy Grant No. DE-SC0016379. This research was partially supported by the Center for Emergent Materials, an NSF MRSEC, under Grant No. DMR-2011876. Electron microscopy was performed at the Center for Electron Microscopy and Analysis (CEMAS) at The Ohio State University.

S.C. synthesized the materials and performed the RHEED, MOKE, and SQUID measurements. N.B. and B.W. performed the TEM and LTEM measurements. C.M.S., Z.L., and S.D. performed the MFM measurements. Z.L. performed MCD measurements. S.C., J.B.F., M.R., and R.K.K. performed micromagnetic simulations. R.K.K., D.W.M., M.R., and P.C.H. conceived the study. All authors participated in data analysis and preparation of the manuscript.

[1] A. Fert, V. Cros, and J. Sampaio, Skyrmions on the track, Nat. Nanotechnol. **8**, 152 (2013).

[2] W. Koshibae, Y. Kaneko, J. Iwasaki, M. Kawasaki, Y. Tokura, and N. Nagaosa, Memory functions of magnetic skyrmions, Jpn. J. Appl. Phys. **54**, 053001 (2015).

[3] G. Finocchio, F. Büttner, R. Tomasello, M. Carpentieri, and M. Kläui, Magnetic skyrmions: From fundamental to applications, J. Phys. D **49**, 423001 (2016).

[4] C. Back, V. Cros, H. Ebert, K. Everschor-Sitte, A. Fert, M. Garst, T. Ma, S. Mankovsky, T. Monchesky, M. Mostovoy, N. Nagaosa, S. Parkin, C. Pfleiderer, N. Reyren, A. Rosch, Y. Taguchi, Y. Tokura, K. von Bergmann, and J. Zang, The 2020 skyrmionics roadmap, J. Phys. D **53**, 363001 (2020).

[5] I. Dzyaloshinsky, A thermodynamic theory of "weak" ferromagnetism of antiferromagnetics, J. Phys. Chem. Solids **4**, 241 (1958).

[6] T. Moriya, Anisotropic superexchange interaction and weak ferromagnetism, Phys. Rev. **120**, 91 (1960).

[7] S. Banerjee, J. Rowland, O. Erten, and M. Randeria, Enhanced stability of skyrmions in two-dimensional chiral magnets with Rashba spin-orbit coupling, Phys. Rev. X **4**, 031045 (2014).

[8] J. Rowland, S. Banerjee, and M. Randeria, Skyrmions in chiral magnets with Rashba and Dresselhaus spin-orbit coupling, Phys. Rev. B **93**, 020404(R) (2016).

[9] R. Wiesendanger, Nanoscale magnetic skyrmions in metallic films and multilayers: A new twist for spintronics, Nat. Rev. Mater. **1**, 16044 (2016).

[10] S. Mühlbauer, B. Binz, F. Jonietz, C. Pfleiderer, A. Rosch, A. Neubauer, R. Georgii, and P. Böni, Skyrmion lattice in a chiral magnet, Science **323**, 915 (2009).

[11] X. Yu, Y. Onose, N. Kanazawa, J. H. Park, J. Han, Y. Matsui, N. Nagaosa, and Y. Tokura, Real-space observation of a two-dimensional skyrmion crystal, Nature (London) **465**, 901 (2010).

[12] C. Moreau-Luchaire, C. Moutafis, N. Reyren, J. Sampaio, C. Vaz, N. Van Horne, K. Bouzehouane, K. Garcia, C. Deranlot, P. Warnicke, P. Wohlhüter, J.-M. George, M. Weigand, J. Raabe, V. Cros, and A. Fert, Additive interfacial chiral interaction in multilayers for stabilization of small individual skyrmions at room temperature, Nat. Nanotechnol. **11**, 444 (2016).

[13] S. Woo, K. Litzius, B. Krüger, M.-Y. Im, L. Caretta, K. Richter, M. Mann, A. Krone, R. M. Reeve, M. Weigand, P. Agrawal, I. Lemesh, M.-A. Mawass, P. Fischer, K. Mathias, and G. S. D.

Beach, Observation of room-temperature magnetic skyrmions and their current-driven dynamics in ultrathin metallic ferromagnets, Nat. Mater. **15**, 501 (2016).

[14] I. Kézsmárki, S. Bordács, P. Milde, E. Neuber, L. Eng, J. White, H. M. Rønnow, C. Dewhurst, M. Mochizuki, K. Yanai, H. Nakamura, D. Ehlers, V. Tsurkan, and A. Loidl, Néel-type skyrmion lattice with confined orientation in the polar magnetic semiconductor GaV_4S_8, Nat. Mater. **14**, 1116 (2015).

[15] X. Yu, N. Kanazawa, Y. Onose, K. Kimoto, W. Zhang, S. Ishiwata, Y. Matsui, and Y. Tokura, Near room-temperature formation of a skyrmion crystal in thin-films of the helimagnet FeGe, Nat. Mater. **10**, 106 (2011).

[16] B. Ding, Z. Li, G. Xu, H. Li, Z. Hou, E. Liu, X. Xi, F. Xu, Y. Yao, and W. Wang, Observation of magnetic skyrmion bubbles in a van der Waals ferromagnet Fe_3GeTe_2, Nano Lett. **20**, 868 (2020).

[17] Y. Wu, S. Zhang, J. Zhang, W. Wang, Y. L. Zhu, J. Hu, G. Yin, K. Wong, C. Fang, C. Wan, X. Han, Q. Shao, T. Taniguchi, K. Watanabe, J. Zang, Z. Mao, X. Zhang, and K. L. Wang, Néel-type skyrmion in WTe_2/Fe_3GeTe_2 van der Waals heterostructure, Nat. Commun. **11**, 3860 (2020).

[18] N. Romming, A. Kubetzka, C. Hanneken, K. von Bergmann, and R. Wiesendanger, Field-dependent size and shape of single magnetic skyrmions, Phys. Rev. Lett. **114**, 177203 (2015).

[19] W. Jiang, G. Chen, K. Liu, J. Zang, S. G. Te Velthuis, and A. Hoffmann, Skyrmions in magnetic multilayers, Phys. Rep. **704**, 1 (2017).

[20] S. McVitie, S. Hughes, K. Fallon, S. McFadzean, D. McGrouther, M. Krajnak, W. Legrand, D. Maccariello, S. Collin, K. Garcia, N. Reyren, V. Cros, A. Fert, K. Zeissler, and C. H. Marrows, A transmission electron microscope study of Néel skyrmion magnetic textures in multilayer thin film systems with large interfacial chiral interaction, Sci. Rep. **8**, 5703 (2018).

[21] S. Schlotter, P. Agrawal, and G. S. Beach, Temperature dependence of the Dzyaloshinskii-Moriya interaction in Pt/Co/Cu thin film heterostructures, Appl. Phys. Lett. **113**, 092402 (2018).

[22] L. Sun, J. Liang, X. Xiao, C. Zhou, G. Chen, Y. Huo, and Y. Wu, Magnetic stripe domains of $[Pt/Co/Cu]_{10}$ multilayer near spin reorientation transition, AIP Adv. **6**, 056109 (2016).

[23] S. Bandiera, R. Sousa, B. Rodmacq, L. Lechevallier, and B. Dieny, Effect of a Cu spacer between Co and Pt layers on the structural and magnetic properties in $(Co/Cu/Pt)_5/Pt$ type multilayers, J. Phys. D **46**, 485003 (2013).

[24] I. Benguettat-El Mokhtari, A. Mourkas, P. Ntetsika, I. Panagiotopoulos, Y. Roussigné, S. Cherif, A. Stashkevich, F. Kail, L. Chahed, and M. Belmeguenai, Interfacial Dzyaloshinskii-Moriya interaction, interface-induced damping and perpendicular magnetic anisotropy in Pt/Co/W based multilayers, J. Appl. Phys. **126**, 133902 (2019).

[25] S. K. Jena, R. Islam, E. Milińska, M. M. Jakubowski, R. Minikayev, S. Lewińska, A. Lynnyk, A. Pietruczik, P. Aleszkiewicz, C. Autieri, and A. Wawro, Interfacial Dzyaloshinskii-Moriya interaction in the epitaxial W/Co/Pt multilayers, Nanoscale **13**, 7685 (2021).

[26] M. Belmeguenai, Y. Roussigne, S. M. Cherif, A. Stashkevich, T. Petrisor, M. Nasui, and M. Gabor, Influence of the capping layer material on the interfacial Dzyaloshinskii-Moriya interaction in Pt/Co/capping layer structures probed by Brillouin light scattering, J. Phys. D **52**, 125002 (2019).

[27] F. Ajejas, Y. Sassi, W. Legrand, S. Collin, A. Thiaville, J. P. Garcia, S. Pizzini, N. Reyren, V. Cros, and A. Fert, Interfacial potential gradient modulates Dzyaloshinskii-Moriya interaction in Pt/Co/metal multilayers, Phys. Rev. Mater. **6**, L071401 (2022).

[28] M. Lonsky, M.-W. Yoo, Y.-S. Huang, J. Qian, J.-M. Zuo, and A. Hoffmann, Structural and magnetic properties of Pt/Co/Mn-based multilayers, Phys. Rev. Mater. **6**, 054413 (2022).

[29] J.-C. Rojas-Sánchez, P. Laczkowski, J. Sampaio, S. Collin, K. Bouzehouane, N. Reyren, H. Jaffrès, A. Mougin, and J.-M. George, Perpendicular magnetization reversal in $Pt/[Co/Ni]_3/Al$ multilayers via the spin Hall effect of Pt, Appl. Phys. Lett. **108**, 082406 (2016).

[30] S. Karayev, P. D. Murray, D. Khadka, T. R. Thapaliya, K. Liu, and S. X. Huang, Interlayer exchange coupling in Pt/Co/Ru and Pt/Co/Ir superlattices, Phys. Rev. Mater. **3**, 041401(R) (2019).

[31] L. Liu, X. Zhao, W. Liu, Y. Song, X. Zhao, and Z. Zhang, Influence of rare earth metal Ho on the interfacial Dzyaloshinskii-Moriya interaction and spin torque efficiency in Pt/Co/Ho multilayers, Nanoscale **12**, 12444 (2020).

[32] S. Cheng, B. Wang, I. Lyalin, N. Bagués, A. J. Bishop, D. W. McComb, and R. K. Kawakami, Atomic layer epitaxy of kagome magnet Fe_3Sn_2 and Sn-modulated heterostructures, APL Mater. **10**, 061112 (2022).

[33] I. M. Billas, A. Chatelain, and W. A. de Heer, Magnetism from the atom to the bulk in iron, cobalt, and nickel clusters, Science **265**, 1682 (1994).

[34] M. Bersweiler, K. Dumesnil, D. Lacour, and M. Hehn, Impact of buffer layer and Pt thickness on the interface structure and magnetic properties in (Co/Pt) multilayers, J. Phys.: Condens. Matter **28**, 336005 (2016).

[35] A. Mukhopadhyay, S. Koyiloth Vayalil, D. Graulich, I. Ahamed, S. Francoual, A. Kashyap, T. Kuschel, and P. Anil Kumar, Asymmetric modification of the magnetic proximity effect in Pt/Co/Pt trilayers by the insertion of a Ta buffer layer, Phys. Rev. B **102**, 144435 (2020).

[36] W. Zeper, F. Greidanus, P. Carcia, and C. Fincher, Perpendicular magnetic anisotropy and magneto-optical Kerr effect of vapor-deposited Co/Pt-layered structures, J. Appl. Phys. **65**, 4971 (1989).

[37] See Supplemental Material at http://link.aps.org/supplemental/10.1103/PhysRevB.108.174433 for additional MOKE, SQUID, and MFM data, an explanation of the LTEM contrast, and details of the micromagnetic simulations.

[38] J. Alameda, F. Carmona, F. Salas, L. Alvarez-Prado, R. Morales, and G. Pérez, Effects of the initial stages of film growth on the magnetic anisotropy of obliquely-deposited cobalt thin films, J. Magn. Magn. Mater. **154**, 249 (1996).

[39] Y. Ochiai, S. Hashimoto, and K. Aso, Co/Pt and Co/Pd ultrathin-multilayered films as new magneto-optical recording materials, IEEE Trans. Magn. **25**, 3755 (1989).

[40] C. J. Lin, G. L. Gorman, C. H. Lee, R. F. C. Farrow, E. E. Marinero, H. V. Do, H. Notarys, and C. J. Chien, Magnetic and structural properties of Co/Pt multilayers, J. Magn. Magn. Mater. **93**, 194 (1991).

[41] X. Wang, Y. Wei, K. He, Y. Liu, Y. Huang, Q. Liu, J. Wang, and G. Han, Effect of the repeat number and Co layer thickness on

the magnetization reversal process in $[Pt/Co(x)]_N$ multilayers, J. Phys. D **53**, 215001 (2020).

[42] X. Wang, A. Cao, S. Li, J. Tang, A. Du, H. Cheng, Y. Sun, H. Du, X. Zhang, and W. Zhao, Manipulating density of magnetic skyrmions via multilayer repetition and thermal annealing, Phys. Rev. B **104**, 064421 (2021).

[43] O. Boulle, J. Vogel, H. Yang, S. Pizzini, D. de Souza Chaves, A. Locatelli, T. O. Menteç, A. Sala, L. D. Buda-Prejbeanu, O. Klein, M. Belmeguenai, Y. Roussigné, A. Stashkevich, S. M. Chérif, L. Aballe, M. Foerster, M. Chshiev, S. Auffret, I. M. Miron, and G. Gaudin, Room-temperature chiral magnetic skyrmions in ultrathin magnetic nanostructures, Nat. Nanotechnol. **11**, 449 (2016).

[44] F. Büttner, I. Lemesh, and G. S. D. Beach, Theory of isolated magnetic skyrmions: From fundamentals to room temperature applications, Sci. Rep. **8**, 4464 (2018).

[45] B. Wang, P.-K. Wu, N. Bagués Salguero, Q. Zheng, J. Yan, M. Randeria, and D. W. McComb, Stimulated nucleation of skyrmions in a centrosymmetric magnet, ACS Nano **15**, 13495 (2021).

[46] M. Benitez, A. Hrabec, A. Mihai, T. Moore, G. Burnell, D. McGrouther, C. Marrows, and S. McVitie, Magnetic microscopy and topological stability of homochiral Néel domain walls in a $Pt/Co/AlO_x$ trilayer, Nat. Commun. **6**, 8957 (2015).

[47] B. Wang, N. Bagués, T. Liu, R. K. Kawakami, and D. W. McComb, Extracting weak magnetic contrast from complex background contrast in plan-view FeGe thin films, Ultramicroscopy **232**, 113395 (2022).

[48] W. Jiang, P. Upadhyaya, W. Zhang, G. Yu, M. B. Jungfleisch, F. Y. Fradin, J. E. Pearson, Y. Tserkovnyak, K. L. Wang, O. Heinonen, S. G. E. te Velthuis, and A. Hoffmann, Blowing magnetic skyrmion bubbles, Science **349**, 283 (2015).

[49] I. Lemesh, K. Litzius, M. Böttcher, P. Bassirian, N. Kerber, D. Heinze, J. Zázvorka, F. Büttner, L. Caretta, M. Mann, M. Weigand, S. Finizio, J. Raabe, M.-Y. Im, H. Stoll, G. Schütz, B. Dupé, M. Kläui, and G. S. D. Beach, Current-induced skyrmion generation through morphological thermal transitions in chiral ferromagnetic heterostructures, Adv. Mater. **30**, 1805461 (2018).

[50] R. Juge *et al.*, Skyrmions in synthetic antiferromagnets and their nucleation via electrical current and ultra-fast laser illumination, Nat. Commun. **13**, 4807 (2022).

[51] A. Vansteenkiste, J. Leliaert, M. Dvornik, M. Helsen, F. Garcia-Sanchez, and B. Van Waeyenberge, The design and verification of MuMax3, AIP Adv. **4**, 107133 (2014).

[52] M. Grimsditch, E. E. Fullerton, and R. L. Stamps, Exchange and anisotropy effects on spin waves in epitaxial Co films, Phys. Rev. B **56**, 2617 (1997).

[53] H. F. Ding, A. K. Schmid, D. Li, K. Y. Guslienko, and S. D. Bader, Magnetic bistability of Co nanodots, Phys. Rev. Lett. **94**, 157202 (2005).

[54] W. Legrand, Y. Sassi, F. Ajejas, S. Collin, L. Bocher, H. Jia, M. Hoffmann, B. Zimmermann, S. Blügel, N. Reyren, V. Cros, and A. Thiaville, Spatial extent of the Dzyaloshinskii-Moriya interaction at metallic interfaces, Phys. Rev. Mater. **6**, 024408 (2022).

[55] H. Jia, B. Zimmermann, M. Hoffmann, M. Sallermann, G. Bihlmayer, and S. Blügel, Material systems for FM-/AFM-coupled skyrmions in Co/Pt-based multilayers, Phys. Rev. Mater. **4**, 094407 (2020).

[56] Appendix, in *Simple Models of Magnetism*, edited by R. Skomski (Oxford University Press, Oxford, 2008), pp. 289–318.

[57] H. F. Ding, W. Wulfhekel, and J. Kirschner, Ultra sharp domain walls in the closure domain pattern of Co(0001), Europhys. Lett. **57**, 100 (2002).

[58] S. P. Vernon, S. M. Lindsay, and M. B. Stearns, Brillouin scattering from thermal magnons in a thin Co film, Phys. Rev. B **29**, 4439 (1984).

[59] X. Liu, M. M. Steiner, R. Sooryakumar, G. A. Prinz, R. F. C. Farrow, and G. Harp, Exchange stiffness, magnetization, and spin waves in cubic and hexagonal phases of cobalt, Phys. Rev. B **53**, 12166 (1996).

[60] G. Shirane, V. Minkiewicz, and R. Nathans, Spin waves in 3*d* metals, J. Appl. Phys. **39**, 383 (1968).

[61] X. Wang, H. Yuan, and X. Wang, A theory on skyrmion size, Commun. Phys. **1**, 31 (2018).